Towards an ab-axis giant proximity effect using ionic liquid gating

Atesci, H.

Chapter 3

Methods of fabrication of *ab*-axis Josephson junctions

The giant proximity effect in cuprate ab-axis Josephson junctions is investigated utilizing a number of methods, namely the gating by means of ionic liquids and etched bilayers. In this chapter, these methods are described along with the pulsed laser deposition technique used for thin film growth.

3.1 Pulsed laser deposition

As described in Chapter 1, in order to investigate the giant proximity effect in the ab-axis properly, an $SS'S$ junction needs to be made. In other words, a lower critical temperature ($T_{c'}$) of an S' area connected to higher T_c S leads. Furthermore, crucial to the making of Josephson junctions is the precise control of growth conditions of the thin cuprate films. For this, we have decided to use pulsed laser deposition (PLD). With the emergence of the laser era in the 1960s, several groups sought to investigate the excitation of atoms and laser-vaporization from solid surfaces [137]. Soon after, attempts were made to flash evaporate ma- terial using the laser as a heat source [138]. Early attempts in 1970s eventually culminated in stoichiometric deposition of multi-component films, such as $YBa_2Cu_3O_7$ films [139], and has since then been successfully utilized to fabricate high quality (epitaxial) ceramic films, ranging from superconductors to ferromagnetic materials.

Although PLD involves a lot of complex physics such as collisional, thermal and electronic excitation, exfoliation and hydrodynamics, in its core, it is a simple technique, using laser pulses to remove material from a target. The absorbed beam energy is converted into thermal, chemical and mechanical energy, which results in electronic excitation of the target surface atoms, and eventually in the ablation of the surface. The ablated material is contained in the form of a highly directional plume, which contains a collection of species, including ions, (clusters of) atoms, microscopic particulates. Once in contact with the surface of the substrate, the adatom essentially feels a hill-valley potential surface along both coordinates parallel to the surface. Initially, the single bond of the adatom with the substrate surface is usually weak, and allows the adatom to change adsorption sites, corresponding to the valleys of the potential surface (see Fig. 3.1). At some point, it can attach itself to another diffusing adatom, forming an island group. The saddle-like potential landscape of the step edges form natural pathways for adatom diffusion, facilitating a growth front of the adatom island. Detachment from the island group is also possible, or even from the surface of the substrate itself. In other cases, adatoms land on the surface of an adatom island, and, similarly to surface diffusion, can diffuse on the island surface. For sufficient diffusion lengths, the adatom can diffuse to the lower layer, called interlayer diffusion.

The deposition parameters are crucial in the nucleation process.

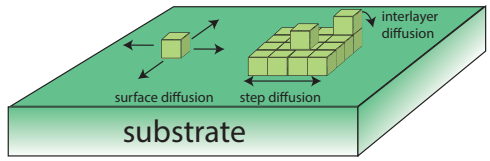

Figure 3.1: A simplified view of adatom dynamics at the substrate surface. Once attached to the surface, the adatom interacts with hill-valey potential landscape of the substrate surface, and can diffuse accordingly if this is energetically favorable. Adatoms can also form islands, the step edges of which form energetically favorable pathways for diffusion, called step diffusion, which facilitates the growth front of the island. Interlayer diffusion is also possible, which is caused by adatomic diffusion to a lower layer of the island.

In view of the vast growth parameter space, however, there is usually no unique set of growth conditions for a specific growth mode of the cuprate. For example, parameters involving the incoming energy of the ablated species, such as the laser fluency and background gas pressure play a role in the crystallinity of the film and the type of growth [140, 141]. Specifically, a higher (lower) laser fluency leads to a higher (lower) nucleation density of adatoms, while increasing (decreasing) the back- ground gas pressure decreases (increases) the landing energy of the ablated material, leading to the other growth modes. Furthermore, the substrate temperature strongly influences the diffusion constant of the adatoms, and therefore the diffusion length scales of adatoms. The temperature should be high enough to ensure adequate atomistic surface mobility at the film growth front. For this reason, an increase in temperature tends to decrease nucleation density and hence influence the growth mode. Parameters relating to the substrate surface, such as termination, miscut angle and roughness also influence the type of growth mode. For cuprate high-T_c superconductors, there is an additional parameter involving the oxygen pressure during deposition, as oxygen is crucial for stoichiometric mass transfer from target to substrate. A too low oxygen pressure can lead to the wrong oxygen stoichiometry and hence charge carrier doping of the film, or can even lead to the decay of the film.

3.1.1 Reflection high energy electron diffraction

Reflection High Energy Electron Diffraction (RHEED) is a tool that is used to in-situ monitor the type of growth mode of crystals. A high energy electron beam at a glancing angle is directed at a sample (see Fig. 3.2). The electrons are diffracted at the surface and then reach the detector, where a diffraction pattern is formed. The spot distribution information is used to analyze the surface morphology of the grown film. As a first step in understanding RHEED, we use the Ewald construction. Starting from a row of atoms along one spatial coordinate, the Fourier transform in k space of this row will be equidistant planes perpendicular to the row [142]. If a sphere is drawn in k space centered on the tip of the incident wave vector k_0, while ignoring the loss of energy and multiple scattering events in the sample surface, there will be some (e.g. k_1 and k_2) diffracted wave vectors having the same magnitude as k_0, satisfying both the elastic scattering and diffraction conditions, which lie on the intersection of the reciprocal lattice planes and the Ewald sphere, i.e. circles. In such a case, there is reflection from the family of direct lattice planes perpendicular to those reciprocal lattice vectors.

If we take the case of a two-dimensional, square lattice surface, the two rows of atoms are rotated 90 degrees from each other. Hence, its Fourier transform is an intersection of planes rotated 90 degrees from each other as well, resulting in reciprocal rods. The intersection of these rods and the Ewald sphere appears as diffraction spots on the fluorescence screen on the circles, known as Laue zones (see Fig. 3.3a). However, diffraction on real samples differs from the ideal, 2D diffraction case. For example, the 2D surface of the substrate is inclined 0.05-0.3 degrees. Furthermore, the growth of cuprates such as $La_{2-x}Sr_xCuO_4$, $Nd_{2-x}Ce_xCuO_4$ and $YBa_2Cu_3O_{7-\delta}$ additionally suffers from surface roughness, finite size domains, and 3D islands, all of which can lead to modifications of the RHEED patterns. In the case of the film having finite-sized domains, the reciprocal rods are widened by an amount which is inversely proportional to the average size of the domains. The intersections of these widened rods with the Ewald sphere are ellipses, leading to a streaked diffraction pattern (see Fig. 3.3b). When the surface is roughened with 3D islands, its reciprocal lattice is the same as that of a 3D crystal, which is a 3D array of reciprocal points. This will give an array of equidistant points in the RHEED pattern (see Fig. 3.3c).

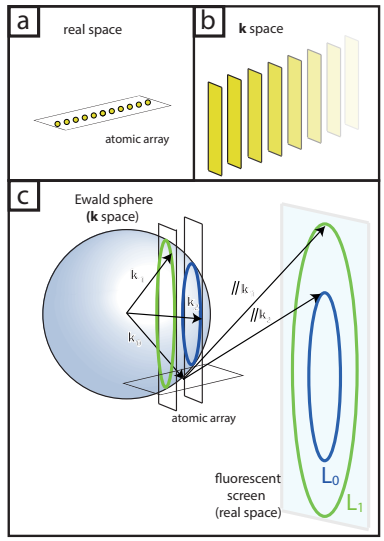

Figure 3.2: **(a)** An array of atoms, when Fourier transformed, gives rise to a series of equidistant planes, or reciprocal lattice planes **(b)**. An incoming beam of electrons of wave vector k_0 gives a diffraction pattern, based on the intersection of the reciprocal lattice planes of the 1D array with the Ewald sphere having a radius of $|k_0|$. These intersections are circles, and the wave vectors from the center of the Ewald sphere to the circles correspond to the wave vectors of the diffracted electrons, in this case k_1 and k_2. **(c)** The circles appear in real space as so-called Laue zones $L_0, L_1, L_2, ...$ when depicted on a fluorescent screen.

3.1.2 Growth modes

As described above, the spatial change of the diffraction pattern can tell something about the surface morphology of the grown film. We can also use the time-dependent change of the RHEED signal to determine what kind of growth modes are present during deposition. The principle behind this is based on diffraction of the electron waves from the surface of the sample. And as is the case for every kind of diffraction phenomenon, the path difference of different electron waves diffracted from the surface can lead to destructive or constructive interference, leading to changes in the intensity of the beam, which is monitored as a function of time. Hence, the time-dependent RHEED signal can be used to distinguish between an atomically flat surface and a stepped surface by measuring the intensity of the specular spot,

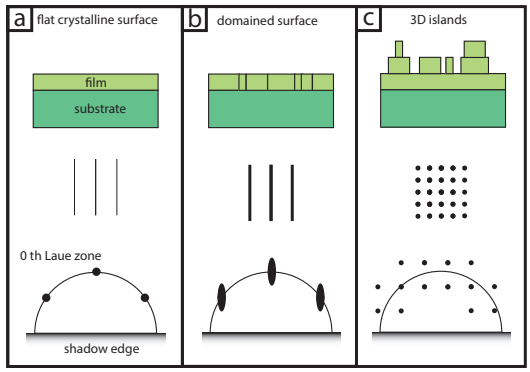

Figure 3.3: **(a)** The Fourier transform of a flat, crystalline surface, is the intersection of the reciprocal planes rotated 90° with respect to each other, i.e. reciprocal rods. The intersection of these rods with the Ewald sphere is a series of points on the 0^{th} Laue zone. **(b)** When some anomaly is introduced in the form of domains, the reciprocal rods are broadened, giving rise to ellipses when intersected with the Ewald sphere, visible as clear strokes on the fluorescent screen. Finally, in the case the surface is coarsened considerably, the diffraction pattern becomes spotty, similar to the 3D array of points in k-space of a bulk crystal **(c)**.

and can thus give an indication of the kind of growth mode present during deposition of the film material. The initial substrate surface is assumed to be flat, as seen in Fig. 3.4a. The incoming beam and the reflected, specular beam at a certain glancing and exit angle θ, are thus reflected from the same atomic plane. The two paths shown always have constructive interference, since there is no path difference between them, enhancing the intensity of the specular spot. Hence, there is an initial maximum in the spot intensity.

During the initial stages of deposition, some 2D islands of deposited material start to form. This introduce a height difference on the initial, flat surface (see Fig. 3.4b), meaning that a part of the specular beam is reflected from the substrate surface, while another is reflected from the 2D island, leading to a path difference between both parts of the beam. At a certain incident angle θ, this can result in destructive interference, leading to a decrease in specular beam intensity. The intensity reaches a minimum when there is a maximum destructive interference due to maximum surface roughness, i.e. when the fractional coverage of monolayers (ML) is 0.5. A continuation in deposition completes the first layer, and hence leads to a

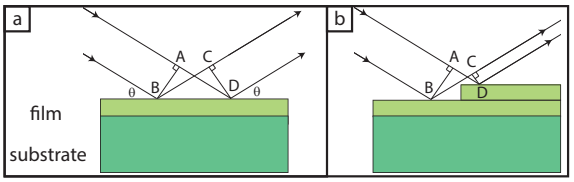

Figure 3.4: **(a)** The two paths of an incoming electron beam at an angle θ are reflected from the same atomic plane of the film. The distances traveled between points A-D and B-C are the same, leading to constructive interference in the specular beam, and hence an enhanced intensity of the specular spot. **(b)** If there is a some surface height difference is introduced by means of deposition, for example, the distances A-D and B-C are not equal anymore. If θ is chosen accordingly, this leads to the specular beam interfering destructively, leading to an decrease in intensity of the specular spot.

maximum in intensity. If we assume this growth mode to be cyclic, in which the next monolayer (ML) is initiated only after the previous layer is fully covered, oscillatory behavior in RHEED intensity is to be expected, with the period of oscillation corresponding to the deposition time needed to complete 1 ML, and more specifically to the time needed to satisfy charge neutrality of the unit cell (UC) [143]. In case of $La_{2-x}Sr_xCuO_4$, for example, this corresponds to 2 periods of oscillation. This type of growth is called layer-by-layer (Frenk-Van der Merve) growth. Layer-by-layer growth mode is stimulated in conditions of relatively high temperature and low oxygen pressure. In such conditions, the nucleation on top of a 2D island is minimized, such that adatoms can migrate to the step edges of 2D islands, and nucleation takes place on fully completed layers, i.e. when both the interlayer diffusion and mobility of adatoms are maximized. Another factor which stimulates layer-by-layer growth mode is minimizing the lattice mismatch between substrate and film.

Changing the experimental growth conditions or increasing the lat- tice mismatch can induce changes in this mode of growth to a 3D island growth mode. A low substrate temperature and high oxygen pressure pressure, diminish the interlayer diffusion and adatom mobility, leading to nucleation also on top of 2D islands. Hence, surface features will become 3D-like, leading to the absence of oscillatory behavior in the RHEED signal after the initial drop in intensity, and giving rise to the aforementioned, spotty RHEED patterns. Most

growth patterns, however, are a combination of both layer-by-layer and island growth, called (Stranski- Krastanov mode). In such a case, the interlayer diffusion is limited due to limitations in surface mobility, resulting in nucleation on top of 2D islands before a UC is completed. During growth, the nucleation and insertion of adatoms at step edges happens at an increasing number of UCs, represented by an exponential dampening of the RHEED oscillations [144] (Fig. 3.5).

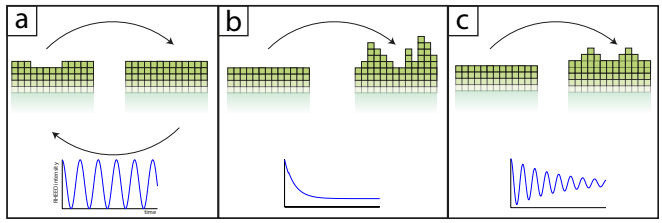

Figure 3.5: **(a)** Layer-by-layer (Frenk-Van der Merve) growth: cyclic process in which the growth of the next layer only starts when the layer before is completed. The RHEED intensity follows a similar behavior, i.e. the maximum intensity appears only when the new layer initiates. The increased adatom density leads to an increased roughness, and hence a decrease in specular beam intensity. The beam intensity recovers when the layer starts to fill up, coupled to a decrease in roughness. **(b)** 3D island growth: process in which rapid coarsening of the surface takes place, leading to the absence of oscillatory behavior in the RHEED intensity. The intensity also drops, coupled to an increased roughness of the surface, enhancing the destructive interference in the specular beam. **(c)**Stranski-Krastanov growth: a process in which the film grows both layer-by-layer and 3D island-like, leading to a dampening in the amplitude of the RHEED oscillations.

3.1.3 Pulsed laser interval deposition

The problem of coarsened surfaces presented by the Stranski-Krastanov growth mode could be easily circumvented by lowering the oxygen background pressure or increasing the deposition temperature. For cuprates, however, these parameters have to be fixed to ensure phase stability. Consequenty, other methods have been tried to manipulate growth. One such method is the Pulsed Laser interval Deposition (PLiD) [144], whereby the interlayer diffusion is optimized due to a decrease of the average island size. This, in turn is connected to increasing the number of nucleation sites by drastically increasing the ablation frequency to accommodate for the exact amount of material needed to complete a UC in a time interval comparable to the

relaxation time. This is typically < 1 s at the typical deposition temperatures used for $La_{2-x}Sr_xCuO_4$, $Nd_{2-x}Ce_xCuO_4$ and $YBa_2Cu_3O_{7-\delta}$. The short-lived interval of deposition is followed by an interval of relaxation for the purpose of recrystallization. This is coupled to the rearrangement of the material, leading to a flatter surface, which in turn provides a more suitable surface for the layer-by-layer growth of the sequential UCs (Fig. 3.6). For the work done in this thesis, the PLiD technique has been used to stimulate 2D layer growth.

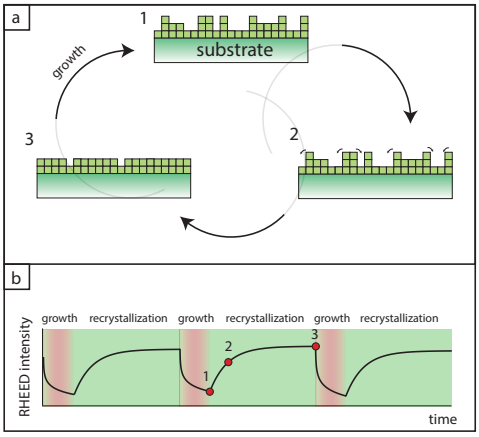

Figure 3.6: **(a)** Pulsed laser interval deposition makes use of the principle of growth interruption. At non-optimal deposition parameters, the growth of a certain amount of material deposition leads to some roughening of the surface (1), which is accompanied by a decrease of the RHEED signal **(b)**. The growth is then interrupted to allow for recrystallization of the film material (2). Eventually, the surface becomes less rough, corresponding to an increased RHEED signal (3). The flatter surface makes a suitable substrate for the next deposition session.

3.2 Pulsed laser deposition setup

All thin films were fabricated in the Thin Film Laboratory at the University of Twente, The Netherlands, using the PLD system. The laser source is KrF excimer-based (Lambdaphysik LPX 210), and has a wavelength of 248 nm, which lies in the range of wavelengths where most metaloxides have their maximum in absorption.The width of the laser pulse is 25 ns. A mask is used to select the middle part of

the laser beam, which is then focused on the target substrate with a lens. The focused beam goes into to the main chamber of the PLD system and ablates the target, which serves as the evaporation source. Both the target and the heater (on which the substrate is glued) are brought in the main chamber via the load lock. Any misalignment is compen- sated by the wobble stick. The heater x, y, z, rotation and azimuth are used to move the heater to its correct position in the chamber. Before deposition starts, the top surface layers of the target material is ablated to remove contaminations. The ablated material hits a shutter instead of the substrate. After this process, the substrate is heated to the deposition temperature, while being in the desired deposition pressure of either Ar, O_2 or O_3. While depositing, the RHEED gun (electron energy of 35 keV) is aimed at the surface with an incident angle of 1 degree. The refracted electron beams are picked up by a fluorescent phosphor screen near the substrate, and is shielded from ablation plumes to reduce contamination. The heater can be rotated in order to adjust the angle of incidence of the electron beam on the substrate. The azimuthal angle can be changed by additional rotation of the heater. A CCD camera monitors the diffraction pattern (Fig. 3.7).

3.3 Growth of thin cuprate films

There are several requirements for achieving a giant proximity effect (GPE) in the *ab*-axis through ionic liquid (IL) gating. As GPE involves pseudogap physics, the first requirement is that the junction area in the *ab*-plane is in its pseudogap phase, while the leads have to be in the superconducting phase. In other words, ΔT_c has to be as high as possible. To achieve this, the junction area $T_{c'}$ has to be as low as possible, while the lead area T_c should be maximized. The former $T_{c'}$ is to be adjusted by means of the Sr and oxygen doping of the film, substrate-film interlayer coupling, and film thickness. The latter T_c is maximized by means of IL gating. We use a solid barrier to separate both the junction and lead areas from IL gating.

3.3.1 Certain considerations for lowering the T_c

In this section, the factors involving lowering the junction $T_{c'}$ are treated. An obvious factor in influencing the $T_{c'}$ of the junction area is the chemical doping of Sr and oxygen of $La_{2-x}Sr_xCuO_{4+\delta}$. As the bulk

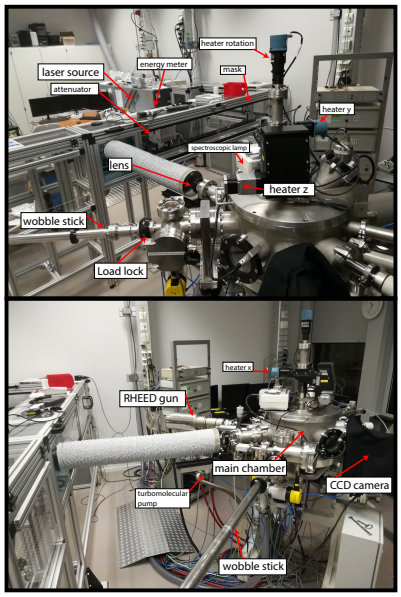

Figure 3.7: The PLD-RHEED system at the Thin Film Laboratory at the University of Twente.

Mott-insulator parent compound is doped, the La^{3+} is replaced by the less positively charged Sr^{2+}. To counteract for this, holes are formed. From $x = 0$ to $x = 0.05$, the properties of an antiferromagnetic Mott-insulator are present. For $0.05 < x < 0.25$ superconductivity appears, with a maximum bulk value of $T_c = 40$ K. For $x > 0.25$, a Fermi liquid behavior is seen [145]. Similar to Sr doping, oxygen overdoping ($\delta > 0$) leads to additional O^{2-} in the UC, which effectively hole dopes the cuprate, and can lead to superconductivity even in the parent compound La_2CuO_4 [146]. Oxygen underdoping ($\delta < 0$) has the opposite effect of effective electron doping and can induce antiferromagnetism in nominally superconducting $La_{2-x}Sr_xCuO_{4+\delta}$ films [147].

Another factor that one can make use of is the fundamental role of interlayer coupling between substrate and film, as it is known that interlayer coupling can play a similar, if not a stronger role in applying an in-plane pressure on the CuO_2 planes [148]. 'Epitaxial pressure' has been successfully applied at $HgBa_2Ca_2Cu_3O_{8+\delta}$ [149], raising the T_c from 133 K to 164 K. In the case of H_2S, hydrostatic pressures of

155 GPa were used to reach a T_c of 203 K, the highest ever reached as of yet [150]. In the case of $La_{2-x}Sr_xCuO_4$, interlayer coupling through compressive strain leads to a T_c as high as 49 K [148]. In our case, however, the goal is not to achieve a maximum T_c but a T_c that is as low as possible while still remaining in the pseudogap phase.

For heteroepitaxial growth of films, the UCs nearest to the interface are strained to accommodate to the lattice mismatch present. As the film thickness is increased, the strain is relaxed as the film thickness increases. The number of UCs that are needed to achieve this state depends on the substrate used. Hence, the film thickness dependence of the in-plane pressure induced by the lattice mismatch can be used to change the T_c of the film. In the case of $La_{1.85}Sr_{0.15}CuO_4$ ($a = 3.78$ Å), films grown on $LaSrAlO_4$ ($a = 3.76$ Å) have shown that a thickness of 500 Å is enough to achieve the same T_c as the bulk value [151], while for those grown on $SrTiO_3$ ($a = 3.91$ Å), thicknesses in the order of 3000 - 4000 Å are required to maximize the T_c [152]. For our purposes of lowering T_c, superconductivity is reported for thin films (2 UC, 26 Å, or more) of $La_{1.85}Sr_{0.15}CuO_4$ grown on $LaSrAlO_4$ [153], while the growth of $La_{1.85}Sr_{0.15}CuO_4$ on $SrTiO_3$ is reported to have superconductivity for films having a thickness of 30 UC, 400 Å, or more [152]. Another important note to be made is that changing the Sr or oxygen doping of the film can change the minimum thickness needed to achieve superconductivity considerably [152].

3.3.2 Substrate choice

$La_{2-x}Sr_xCuO_{4+\delta}$ has a pseudotetragonal structure with an in-plane lattice constant of 3.78 Å. For epitaxial film growth, its substrate coun- terpart should be having a comparable lattice constant as well. There are several possibilities, such as $(LaAlO_3)_{0.3}(Sr_2AlTaO_6)_{0.7}$ (+2.4 %), $LaSrAlO_4$ (-0.5 %), and $SrTiO_3$ (+3.4 %). Using the latter substrates leads to tensile strain in the grown films. The former substrate would lead to compressive strain. Although $SrTiO_3$ has been used as a substrate for $La_{2-x}Sr_xCuO_4$ growth [81], it can easily become conducting during processing, such as argon ion etching. For this reason, this substrate is not preferred. The substrate $(LaAlO_3)_{0.3}(Sr_2AlTaO_6)_{0.7}$ does not become conducting after etching processes, and is hence usable. An added benefit is that the Czochralski growth of the source crystals of $(LaAlO_3)_{0.3}(Sr_2AlTaO_6)_{0.7}$ generally yields a cleaner material with less defects than the flame fusion

(Verneuil) growth of $SrTiO_3$. The substrate material $LaSrAlO_4$ is the most suitable for layer-by-layer growth and maximizing the T_c of due to compressive strain induced in $La_{2-x}Sr_xCuO_4$ [152, 154]. The effect of mismatch in lattice parameters can be seen in the specular beam intensity characteristics (Fig. 3.8a). The growth of $La_{2-x}Sr_xCuO_4$ on $LaSrAlO_4$ compared to that on $(LaAlO_3)_{0.3}(Sr_2AlTaO_6)_{0.7}$ shows that RHEED oscillation amplitude is conserved for a longer time, until the 30^{th} UC. For $(LaAlO_3)_{0.3}(Sr_2AlTaO_6)_{0.7}$, however, the transition to a 3D growth mode typically happens at around the 10^{th} UC.

The $(LaAlO_3)_{0.3}(Sr_2AlTaO_6)_{0.7}(001)$ substrate is annealed at a temperature of 1050 C for 10 h under an O_2 flow of 150 ml/min. This results in clear steps on the surface, the average terrace width of which coincides with the miscut angle of the surface. The height difference between nearest neighbour terraces is 3.4 Å, which corresponds to the cubic UC parameter of $(LaAlO_3)_{0.3}(Sr_2AlTaO_6)_{0.7}$. This is an indication that the surface is mainly single terminated, as is confirmed in other reports which mention that more than 90 % of the surface belongs to the $AlO_{2-\delta}/TaO_{2-\delta}$ termination after an annealing procedure [155] (Fig. 3.8c). In the case of $LaSrAlO_4(001)$, an annealing treatment is not essential in achieving 2D layer growth [10, 156], while some reports do mention annealing treatments for the growth of $SrRuO_3$ [157] or $YBa_2Cu_3O_7$ films [158]. It must be noted that most of our $LaSrAlO_4$ have not been annealed, while those that were, were exposed to an annealing procedure at 1050 C for 10 h under an O_2 flow of 50 ml/min. Such an annealing procedure gives rise to a surface of double termi- nation, as is seen in (Fig. 3.8c). This is evident from the step heights equaling half the c axis lattice parameter (6.3 Å) of $LaSrAlO_4$.

The smaller in-plane lattice parameter of $LaSrAlO_4$ also has an effect on the superconducting properties of the film. As expected, the compressive strain leads to the film being on the verge of superconductivity for $x = 0.05$. For $(LaAlO_3)_{0.3}(Sr_2AlTaO_6)_{0.7}$, the doping has to be increased to 0.07 to get the same characteristics (Fig. 3.8b) due to substrate-film interlayer stress.

3.3.3 $La_{2-x}Sr_xCuO_{4+\delta}$ growth

$La_{2-x}Sr_xCuO_4$ films are grown at 740 C by means of pulsed laser deposition with an energy density of 1.3 - 1.65 J/cm^2, spot size of 1.36 mm^2, and a repetition rate of 1-4 Hz in an O_2 atmosphere (p_{O_2} ≈1.3×10^{-1}

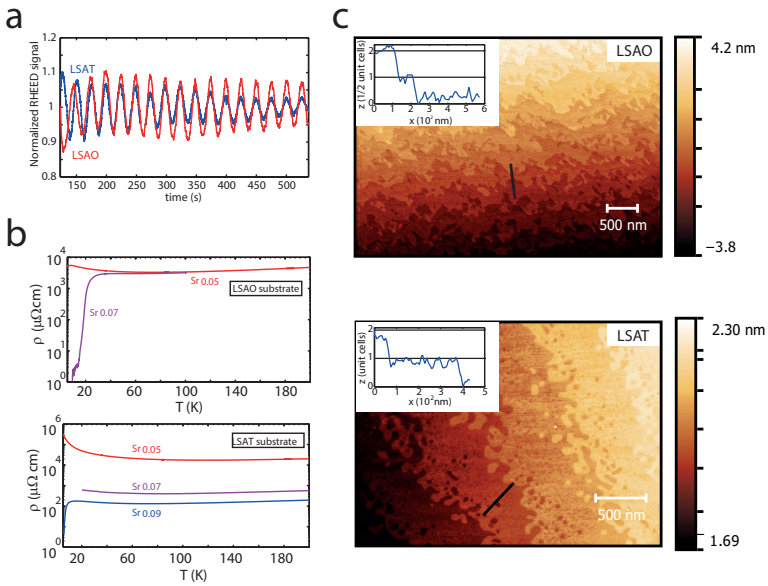

Figure 3.8: **(a)** Normalized RHEED signal vs. time for $La_{1.95}Sr_{0.05}CuO_4$ growth on $LaSrAlO_4$ (LSAO) and $(LaAlO_3)_{0.3}(Sr_2AlTaO_6)_{0.7}$ (LSAT). The RHEED oscillation amplitude in the former case is preserved over a substantially larger amount of oscillations than in the latter case. **(b,top)** $\rho(T)$ characteristics for different levels of Sr doping of a 30 UC film grown on $LaSrAlO_4$. For $x = 0.05$ the film is on the verge of being a superconducting at 4 K. Increasing the doping to $x = 0.07$ induces a superconducting transition, with a $T_{c,mid}$ of 20 K. When grown on $(LaAlO_3)_{0.3}(Sr_2AlTaO_6)_{0.7}$ (b,bottom), former two doping levels are insufficient to induce a superconducting transition, for which a doping of $x = 0.09$ is needed. **(c,top)** Atomic force microscopy (AFM) scan of an annealed surface of $LaSrAlO_4$, which has double termination. Inset: the steps indicate that the height difference between the next-neighbour terraces is equal to $\frac{1}{2}\times c$-axis lattice parameter of $LaSrAlO_4$, namely 6.3 Å. Annealed $(LaAlO_3)_{0.3}(Sr_2AlTaO_6)_{0.7}$ **(c,bottom)** typically shows full UC steps of 3.4 Å.

mbar). The target-substrate distance is kept at 47 mm, at which on average 95 pulses were needed to complete one UC, comparable to previous reports [81], as is monitored by means of RHEED (see Fig. 3.9). After deposition, the sample is kept at the deposition temperature and pressure for 15 minutes. Then, the O_2 pressure in the chamber is increased to 1 bar. This atmosphere is used to anneal the sample for 15 minutes at 600 C and 30 minutes at 450 C, while maintaining a cooldown rate of 10 K/min. The oxygen annealing are meant to give the $La_{2-x}Sr_xCuO_4$ films the correct oxygen stoichiometry, i.e. δ =0.

By adjusting the annealing times, one can either overdope ($\delta > 0$) or underdope ($\delta < 0$) the film. We have hence used oxygen doping, along with Sr doping, as means of influencing the T_c of the film [81, 147]. Table 3.1 lists some of the film properties and deposition parameters for samples with a finite T_c.

Sample number	Substrate	x	d (UC)	t at 600 C (min.)	t at 450 C (min.)	$T_c(R=0)$ (K)
LSCO45	LSAO	0.07	13	15	30	5.7
LSCO47	LSAO	0.07	10	15	20	1.5
LSCO48	LSAO	0.07	10	15	20	3.9
LSCO57	LSAT	0.09	30	15	30	3.5
LSCO58	LSAT	0.09	30	15	30	1.0
LSCO61	LSAT	0.09	30	15	30	3.5
LSCO62	LSAT	0.09	30	15	30	2.9
LSCO64	LSAT	0.09	30	15	30	4.0
LSCO66	LSAT	0.09	30	15	30	2.0
LSCO69	LSAT	0.09	30	15	30	5.5
LSCO74	LSAT	0.09	30	15	30	1.0
LSCO80	LSAT	0.09	30	15	30	5.1

Table 3.1: List of samples having an initial T_c used for the purpose of investigating the giant proximity effect by means of IL gating. Other parameters include the substrate type $(LaAlO_3)_{0.3}(Sr_2AlTaO_6)_{0.7}$ (LSAT) or $LaSrAlO_4$ (LSAO), film thickness d, annealing times t at 600 and 450 C.

3.3.4 Growing highly crystalline $La_{2-x}Sr_xCuO_4$ films

The crystallinity of the surface is key in acquiring the optimal electrostatic charge transfer in the film, as was found in IL gated FeSe films [92]. The layer-by-layer growth of $La_{2-x}Sr_xCuO_4$ can be optimized using a metallic buffer layer, based on the recipe used by Bozovic *et al.* [10, 64]. The advantage of this metallic buffer layer is the intrinsic offset in lattice parameters of $LaSrAlO_4$ and $La_{2-x}Sr_xCuO_4$ and a difference in thermal expansion coefficients ($\alpha = 8.5 \times 10^{-6}K^{-1}$ for $La_{2-x}Sr_xCuO_4$ and $\alpha = 10.5 \times 10^{-6}K^{-1}$for $LaSrAlO_4$) that lead to a crossover of lattice constants at typical growth temperatures happens at a doping level of $x = 0.40$-0.45 [148]. The perfect match in the lattice constants of both the $LaSrAlO_4$ substrate and buffer film in turn provides excellent growth conditions for subsequent layers, as has been shown before in Ref.10.

The unbuffered film follows the double termination of the $LaSrAlO_4$ substrate surface (fig. 3.10a), which results in the formation of grain boundaries at the terraces (fig. 3.10b). This is confirmed by the broad-

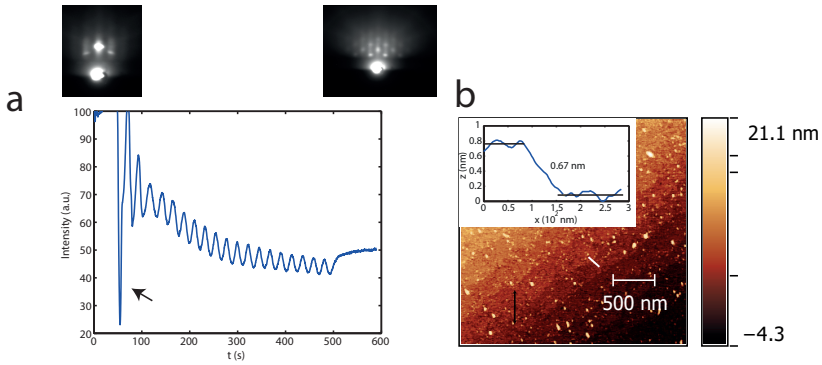

Figure 3.9: **(a)** RHEED signal vs. time for $La_{1.95}Sr_{0.05}CuO_4$ layer-by-layer growth on a non-annealed $LaSrAlO_4$ substrate, showing clear RHEED oscillations of half UC monolayers until the end of the deposition. The arrow indicates a manual increase in the beam intensity. The left and right insets show the RHEED patterns of the $LaSrAlO_4$ substrate, and of the resulting film, respectively. The final RHEED pattern appears to have extra spots next to the clear two-dimensional spots, indicating surface roughening and a transition to 3D growth. **(b)** AFM image of a 10 UC thick layer-by-layer grown $La_{1.95}Sr_{0.05}CuO_4$ film on $LaSrAlO_4$. The inset shows a step height of 6.7 Å, which is half the c axis lattice parameter of the substrate $LaSrAlO_4$, indicating layer-by-layer growth. The surface roughness is comparable to the initial substrate roughness, 4.0 Å.

ened 2D RHEED patterns, indicative of a domained surface, as is discussed in Section 3.1.2. In contrast, the insertion of a $x = 0.30$ buffer layer (due to a lack of target availability of a higher Sr doping) leads to atomically flat terraces, not containing grain boundaries and hence are not influenced by the double termination (fig. 3.10). After growth, the 2D RHEED spots are still clearly visible, indicating a crystalline, 2D surface. The crystalline quality of the films resemble the molecular beam epitaxy grown $La_{2-x}Sr_xCuO_4$ of Bozovic *et al.* [10]. Another observation is that the amount of pulses (i.e. 90) typically needed to complete the first UC of the $x = 0.30$ buffer layer is significantly higher than the pulses (i.e. 81) needed in the subsequent layers. Combined with the previous observation of flat terraces, it could be assumed that the mixed termination at the surface of $LaSrAlO_4$ containing AlO_2/(Sr,La)O, is not equally distributed at the terrace, but is dominant (∼70-80%/20-30%) in one of the two terminations. We hence suspect that the initial extra pulses needed for the completion of the metallic buffer layer involves the filling up of the non-dominant

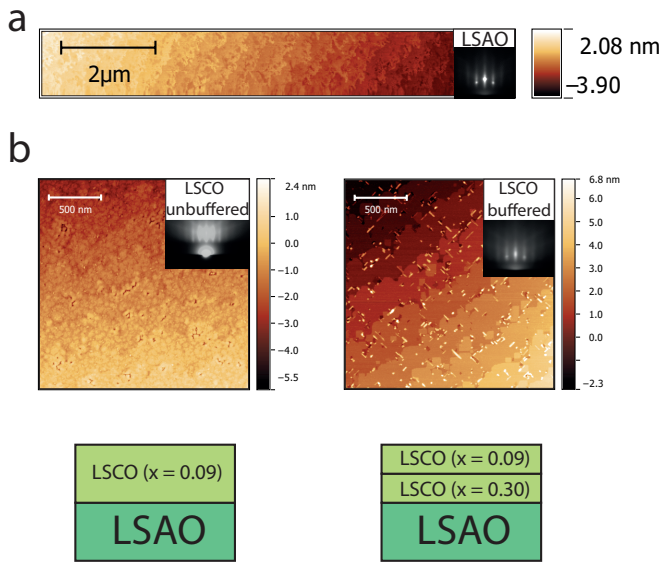

Figure 3.10: **(a)** Shows a typical AFM image of a double-terminated $LaSrAlO_4$ (LSAO) surface. The terminations of AlO_2 and (Sr,La)O are not equally distributed, but is dominant (∼70-80%/20-30%) in one of the two terminations. **(b)** The AFM images of an unbuffered and buffered $La_{2-x}Sr_xCuO_4$ (LSCO, $x = 0.09$) film. Here, the buffered film is grown on a metallic $x = 0.30$ layer of 1 UC thick. Both films have the same total thickness, in this case 7 UC. The morphology of the unbuffered films follow the double-termination of the substrate, and is hence characterized by a domained surface. This is in line with the typical broadening observed in the 2D RHEED spots, which, as discussed in Section 3.1.2, is an indication of a domained surface. In contrast, the enhanced crystalline quality of the buffered films is accompanied by the absence of grain boundaries and a domained surface, as is accompanied by clear 2D RHEED spots.

termination.

The transport properties of the layers grown with and without a metallic buffer layer tend to be different as well. Without a metallic buffer layer, the strain effects result in a semiconducting behavior, as is seen for the films of 7 UC (fig. 3.11a). Insertion of a mere 1 UC buffer layer changes the transport properties completely and superconducting transition temperatures higher than those for bulk can be observed (fig. 3.11a and b).

It is unlikely that the high T_c is caused by an overdoping of oxygen

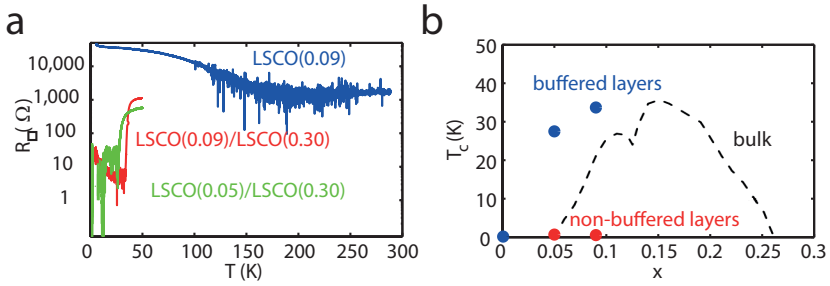

Figure 3.11: **(a)** $R(T)$ curves of various doping levels of $La_{2-x}Sr_xCuO_4$ (LSCO) of a total thickness of 7 UC. The unbuffered film shows the expected semiconducting behavior, while the insertion of a buffer layer of 0.30 leads to superconductivity. The doping levels are parenthesized. **(b)** The T_c values induced in the buffered films are much higher than attainable in the non-buffered films, or bulk material.

in the buffered films, as the recipe used during deposition is meant for optimal stoichiometric oxygen content. In theory, cation intermixing could occur [159] over distances of at most 1 UC and would give a maximum T_c for the $La_{1.7}Sr_{0.3}CuO_4/La_2CuO_4$, as the interface would then be optimally doped. This, however, is not observed.

One likely scenario is that of strain, based on the observation that a films of 3 UC or less do not become superconducting. At the same time, this shows that the large T_c cannot be caused by the $x = 0.30$ layer itself.

Another scenario deals with the preformed pairs interpretation of the pseudogap phase. In this picture, the electron pairing in the $x = 0.09$ layer cannot lead to superconductivity due to a lack of phase coherence, as the superfluid density is too low [32]. The proximity of the $x = 0.09$ layer to the phase coherent, metallic $x = 0.30$ layer then should effectively lead to a phase coherence in the $x = 0.09$ layer as well, leading to an increase in T_c. Interestingly, similar observations have been made with experiments concerning similar metallic and underdoped $La_{2-x}Sr_xCuO_4$ bilayers [23]. A future study would be needed for a more thorough investigation of these T_c raising effects in bilayers, and their relationship to the giant proximity effect.

3.4 $Nd_{2-x}Ce_xCuO_{4-\delta}$ growth

The electron doped cuprate $Nd_{2-x}Ce_xCuO_{4-\delta}$ is part of the family of electron-doped superconductors of the 214-system $Re_{2-x}Ce_xCuO_{4-\delta}$ with Re = Nd, Pr, La, Sm, Eu, or Gd. Just like its hole-doped counterpart $La_{2-x}Sr_xCuO_{4+\delta}$, the superconductivity depends on both its second rare-earth element, Ce(x), and oxygen content. The maximum T_c appears at Ce = 0.15 and δ = 0.04, pointing to the fact that $Nd_{2-x}Ce_xCuO_4$ has to be oxygen reduced. For this, an in-situ post-annealing treatment in vacuum is done at 750 C for 8 minutes at a pressure of 1×10^{-7} mbar. $Nd_{2-x}Ce_xCuO_4$ has an in-plane lattice parameter of 3.95 Å, for which $SrTiO_3$ (+0.9 %) as a substrate would be most suitable for heteroepitaxial growth. However, because of the possibility of inducing oxygen vacancies during processing, we decided to use the larger mismatched annealed $(LaAlO_3)_{0.3}(Sr_2AlTaO_6)_{0.7}$ as a substrate (+2.0 %). To compensate for the stress induced by the larger mismatch of the $(LaAlO_3)_{0.3}(Sr_2AlTaO_6)_{0.7}$ substrate, undoped buffer layers have been used to release stress in the doped top layers, similar to bilayer concepts used in other works [10, 81, 154]. During deposition, the oxygen background pressure is 0.25 mbar, the sample temperature is 820 C, while the target-substrate distance is held at 52 mm. Furthermore, the laser fluence is 1.2 J/cm^2 while maintaining a repetition rate of typically 1-4 Hz. Occasionally, growth interruption was applied to stimulate layer-by-layer growth. When monitored with RHEED, only a few oscillations are observable initially, suggesting a limited 2D growth mode, quickly followed by 3D island growth, as is suggestive by the spotty RHEED patterns. When checked by AFM, the surface suggests island growth (Fig. 3.12), as has been seen before in $Nd_{2-x}Ce_xCuO_4/SrTiO_3$ films [160] and heteroepitaxial growth of other cuprates, such as $YBa_2Cu_3O_{7-\delta}$ [161].

3.5 Contact resistance and barrier characterization

The contact resistance $I(V)$ characteristics show non-linearity in the case Ti is sputtered ex-situ on $La_{1.95}Sr_{0.05}CuO_4$ (20 UC) as a wetting layer before Au deposition, indicating a non-Ohmic contact (see Fig. 3.13). The interface between a metal and a p-type semiconductor can form a Schottky-type barrier if the work function of the metal

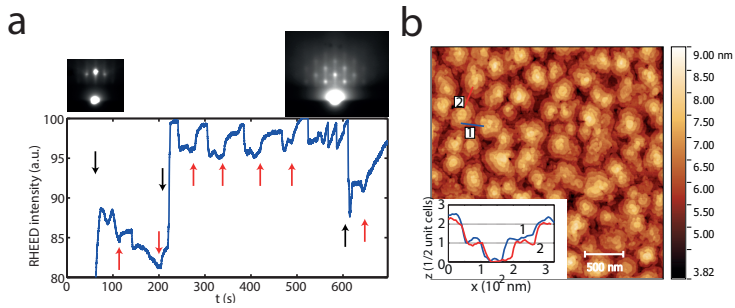

Figure 3.12: **(a)** RHEED signal vs. time for $Nd_{1.95}Ce_{0.05}CuO_4$ growth on an annealed $(LaAlO_3)_{0.3}(Sr_2AlTaO_6)_{0.7}$ surface. The black and red arrows represent manual augmentation of the beam intensity, and growth interruption, respectively. The RHEED data in between the arrows show slight oscillatory behavior, typical of the island-like growth exhibited by $Nd_{1.95}Ce_{0.05}CuO_4$. The initial substrate surface of annealed $(LaAlO_3)_{0.3}(Sr_2AlTaO_6)_{0.7}$ shows clear two-dimensional spots, while the spotty behavior of the RHEED pattern after growth is another indication of the presence 3D islands. **(b)** The AFM image of a 30 UC thick $Nd_{1.95}Ce_{0.05}CuO_4$ film on $(LaAlO_3)_{0.3}(Sr_2AlTaO_6)_{0.7}$, the surface of which is island-like. The inset shows height steps corresponding with half the c axis lattice parameter of $Nd_{1.95}Ce_{0.05}CuO_4$, 6.5 Å.

is larger than that of the semiconductor. Since $La_{2-x}Sr_xCuO_4$ is a p-type conductor and has a relatively large work function (5.06 eV for Sr 0.05 doping) [162], most metals like Ti (4.33 eV) do not form an Ohmic contact with the cuprate. The contact is worsened by the fact that Ti can draw away oxygen from the cuprate, as it is prone to form TiO_2. Oxygen-deficient $La_{2-x}Sr_xCuO_4$ can lose its superconductive properties, hence rendering such a sample unusable. Exposure to air during transport from the PLD setup to the sputtering setup can either cause an adsorbate layer to form on the cuprate, or can cause the CO_2 and H_2O in the air to react with the top layer [163], causing a so-called dead layer. The $I(V)$ curve can be fitted using a polynomial of the form $I(V) = \alpha V + \gamma V^3$, based on Simmons model for metal/insulator/metal junctions for low voltages [164]. Here, J is the current density $\alpha = A\left(\frac{e}{h}\right)^2 \frac{\sqrt{2m_e\phi}}{d} e^{-\beta\sqrt{\phi}}$, and $\frac{\gamma}{\alpha} = \frac{(\beta e)^2}{96\phi} - \frac{\beta e^2}{32\sqrt{\phi}}$. Here, A, e, h, m_e represent the metal/insulator/metal junction contact area, the electron charge, Planck constant and the electron mass. Furthermore, ϕ is the average barrier height across the barrier thickness d, while $\beta = 4\pi A\sqrt{2m_e}d/h$. The fitparameters d and ϕ correspond to 1.1

nm and 0.61 eV. These numbers roughly correspond to the thickness of the Ti adhesion layer (1-2 nm), and the difference in work function of Ti and $La_{2-x}Sr_xCuO_4$ (0.73 eV).

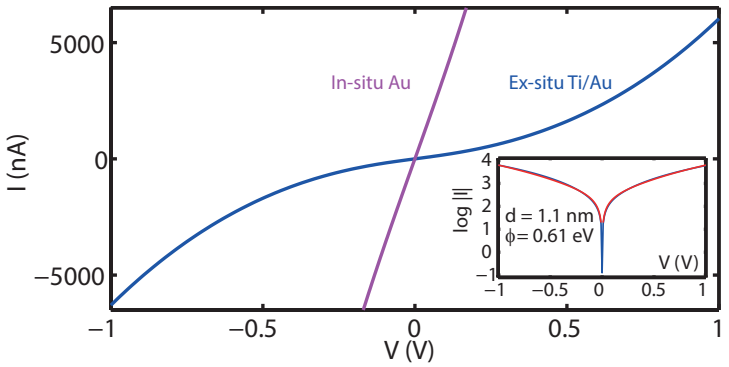

Figure 3.13: Two-point $I(V)$ curves for $La_{1.95}Sr_{0.05}CuO_4$ (20 UC) for which the contacts were applied by means of ex-situ Ti/Au (blue) and in-situ Au (purple) deposition. Inset: log|I| plot for the Ti/Au contacts. The fitparameters are based the Simmons model, corrected for the junction contact area of Ti to $La_{2-x}Sr_xCuO_4$ (approx. 1 mm^2)

The barrier has an insulating behavior when cooled down to low temperatures, and typically rendered the sample unmeasurable below 100 K. To counter this problem, we have tried sputtering without Ti adhesion layer, as Au has a work function that is sufficiently high (5.1 eV) [165]. However, the adsorbate layer formed during ex-situ transporta- tion makes it difficult for Au to adsorb at the surface of the cuprate, resulting in the removal of the sputtered Au during the lift-off process. We solve this by depositing Au in-situ by means of PLD, following the cuprate deposition. As the Au covers the whole substrate, structuring the sample to expose the $La_{2-x}Sr_xCuO_4$ surface for ionic liquid gating should involve removing the parts of the Au. This can be done by Ar ion etching, as is done by [10]. This is cumbersome, and can risk damaging the cuprate layer, and removing oxygen from its lattice structure, rendering it non-superconducting. Using a $KI/H_2O/I_2$ solution in 4:1:40 mass ratio induces a ionization reaction of Au, which subsequently dissolves in the solution, but leaving the $La_{2-x}Sr_xCuO_4$ layer intact. Compared with the non-linear $I(V)$ characteristic of ex-situ deposited Ti/Au, the typical $I(V)$ characteristic of

samples prepared with in-situ Au deposition is nearly perfectly linear and metallic.

3.6 Methods related to ionic liquid gating

As described in Chapter 2, the electric double layer concept of IL gating has major advantages when compared to standard oxide field effect transistors. However, ILs can be contaminated quickly, as impurities from the air such as H_2O and O_2 easily dissolve in the IL, even in hydrophobic ones. These molecules are electroactive and affect gating performance, and their removal from the IL is essential before any voltammetric measurement. The electroactive nature of H_2O and O_2 shift the cathodic (anodic) limiting potential of the sample towards the positive (negative) potential, essentially limiting the electrochemical window (EW) of the IL.

Hence, the partial pressure of these molecules has to be minimized. For this, in our experiments we developed the practice that the bottle in which the IL is kept, is stored in a N_2 atmosphere of a glove box, while the IL interaction time with ambient air is kept at a minimum, typically a minute or so. Furthermore, with the sample in place the IL is vacuum dried at pressures varying between 1×10^{-5} and $\times10^{-6}$ mbar for 15 minutes or more, making p_{O_2} and p_{H_2O} in the order of $\times10^{-7}$ mbar.

Yet another way of optimizing IL gating of a material is to have its surface free of contaminations as much as possible. If the surface is contaminated with residuals from structuring processes, a barrier between the IL and the material surface is formed, effectively increasing the electric double layer distance, and hence the field effect induced. Before any gating experiments, the surface of the material is cleaned by an alcohol wetted lens tissue or by means of irradiation with UV light from a mercury lamp under air. The 184.9 nm wavelength generated by the lamp is adsorbed by oxygen, leading to generation of ozone, while the 253.7 nm wavelength is adsorbed by ozone. Hence, ozone is continually formed and destroyed, an intermediate product of which is atomic oxygen. Atomic oxygen is a strong oxidizing agent, which reacts with the molecules that originate from any process residuals, such as PMMA or photoresist. This process, can give clean surfaces without affecting the oxygen doping of the cuprate itself. We have observed no changes in superconducting

properties of $La_{2-x}Sr_xCuO_4$ films for illumination times as long as 90 minutes. Although the oxygen concentration in the $La_{2-x}Sr_xCuO_4$ films can also be modified by the ozone exposure, this requires the treatment to be done at elevated temperatures [113].

3.7 Introducing an *ab*-axis Josephson junction

To prevent the junction area from being gated along with the lead areas, a barrier is necessary. The barrier needs to fulfill a number of requirements. Firstly, the barrier should be insulating, so no parallel conduction path is formed. Secondly, IL gating across the barrier should not influence the layer below it electrostatically. For this, the induced charge carrier density in the layer beneath has to be minimized, defined as

$$\sigma = \int_0^{V_g} \frac{\epsilon_0 \epsilon_I(V)}{d} dV \tag{3.1}$$

Here, ϵ_0 is the dielectric constant of free space, ϵ_I is the dielectric constant of the insulator, d is the thickness of the insulator, and V_g is the gate voltage. To minimize σ, the main parameter that can be tweaked is d, which has to be maximized. As the electric double layer separation in IL gating experiments is typically 1 nm [122], if the barrier thickness is added to this separation, the field effect can quickly become negligibly low. In contrast, V_g in theory should be kept at a minimum, but is typically is not kept at a minimum. Furthermore, ϵ_I is preferably kept as low as possible, while not much flexibility exists in this parameter space, as typical oxide insulator materials such as $SrTiO_3$, TiO_2, $(LaAlO_3)_{0.3}(Sr_2AlTaO_6)_{0.7}$, $LaAlO_3$ and Al_2O_3 have a relatively large dielectric constant (310, 170, 22.7, 23.5, ∼9, respectively, at room temperature).

Thirdly, the barrier should be electrochemically neutral towards the junction area. In many cases of off-stoichiometric growth of the barrier material, the unbalance is compensated by diffusion of certain species from the junction area to the barrier. As an example, some oxide and nitride barriers such as SiO_2 [81] and SiN_3 tend to influence the oxygen doping of the material when not grown stoichiometrically, leading to unintentional changes in the T_c of $La_{2-x}Sr_xCuO_4$, as the T_c of $La_{2-x}Sr_xCuO_4$ is dependent on its oxygen content. This process is usually a very slow one, making the junction unmeasurable in a time period of an order of a week. Lastly, the barrier should be

impermeable to ions, such as oxygen, but also the anions and cations of the ionic liquid. For example, the oxide material $PbBa_2Cu_3O_7$ as a barrier has been proven to facilitate oxygen migration between the cuprate $YBa_2Cu_3O_7$ and ionic liquid [63].

Taking all of these considerations into account, we have chosen to primarily work with Al_2O_3, although, as we will see in Chapters 8 and 9, there are still some issues which make it problematic as a barrier material. Although this material has a large dielectric constant as is mentioned before, the reports of its impermeability to oxygen ion diffusion [63] made it an attractive material to work with. Some reports mention oxygen diffusion from the $La_{2-x}Sr_xCuO_4$ when Al_2O_3 is grown at elevated temperatures (300 C) in combination with a cooling procedure in 1 bar of O_2 [81]. To limit any such interaction between oxygen in the Al_2O_3 and $La_{2-x}Sr_xCuO_4$, the deposition of AlO_x is done at room temperature.

Depending on the kinetic energy of the ablated species, pulsed laser deposition growth of AlO_x can lead to a number of morphological phases of AlO_x (see Fig. 3.14a), expressed in $\sqrt{p}d$ in Ref. 166, where p is the oxygen background pressure and d is the target-substrate distance. Provided the kinetic energy is low (high O_2 background pressure, large target-substrate distance, and small laser fluence), the grown AlO_x is open and porous, for which x is close to the stoichiometric value of 1.5. When deposited at 2×10^{-1} mbar of O_2 pressure, $d = 60$ mm and $E = 1.5$ J/cm^2, $\sqrt{p}d$ becomes 0.33 Pa$^{0.5}$m, which is a transitional regime between both ends of the morphology spectrum. As expected, the typical film morphology is relatively coarsened and possibly porous, as shown in the AFM image (see Fig. 3.14b,i). As shown in Fig. 3.14c, the AlO_x layer has little influence on the T_c and general $R(T)$ characteristics of the $La_{2-x}Sr_xCuO_4$ film. However, because of its possible porous character, it is not recommended for IL gating experiments.

Lowering the background pressure to 1×10^{-2} mbar and minimizing d to 42 mm leads to a substantial increase of the kinetic energy of the incoming species. In this case $\sqrt{p}d = 0.03$ Pa$^{0.5}$ m, which is sufficiently low for dense film growth (see Fig. 3.14). The dense film surface shows the same roughness as the substrate on which it is grown when scanned by AFM, suggestive of a very flat film, to such an extent that the film morphology follows the terrace steps of the $(LaAlO_3)_{0.3}(Sr_2AlTaO_6)_{0.7}$ substrate (see Fig. 3.14b,ii). Although

the dense film has a stoichiometric value close to 1 [166], it has little influence on the $R(T)$ characteristics of the $La_{2-x}Sr_xCuO_4$ film, suggestive of limited oxygen diffusion out of the film. Hence, the inherent dense film properties and its limited influence on $La_{2-x}Sr_xCuO_4$ make it an ideal barrier material for IL gating.

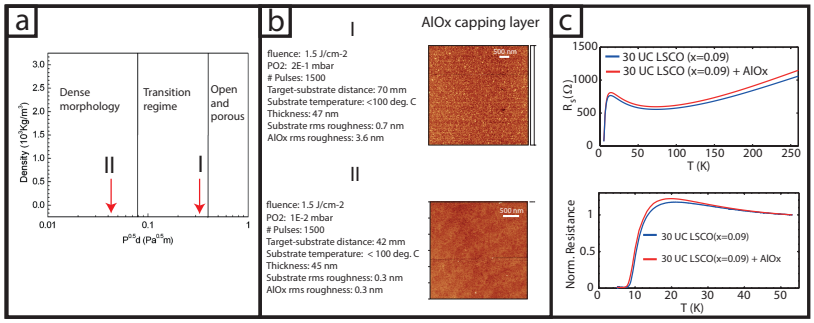

Figure 3.14: **(a)** Film density vs. $\sqrt{p}d$ for different morphological regimes of AlO_x, based on Ref.166. For high kinetic energy of the incoming particles, the film is dense, whereas an open and porous film is obtained for low kinetic energies. **(b)** AFM images of AlO_x layers I and II grown in the intermediate and dense regime, respectively. Layer I shows a coarsened surface, while layer II shows a flat surface. Both layers I (**c,top**) and II (**c,bottom**) do not affect the $La_{2-x}Sr_xCuO_4$ substantially in T_c.

3.8 Attaining $SS'S$ junctions by means of etched bilayers

As is mentioned in Section 1.4, obtaining a giant proximity effect through etched bilayers requires a few conditions to be met. Firstly, a $T_{c'}$ should be present in the bottom film, which preferably should be as low as possible. Secondly, the T_c of the top layer should be as high as possible. These requirements are similar to those of the IL-induced giant proximity effect, except that in this case, the T_c difference is already present and is exploited by means of an etched structure. This method allows the top layer to be different than the bottom layer. Hence, bilayers have been made by (1) making use of different Sr levels of $La_{2-x}Sr_xCuO_4$ and (2) making use of $YBa_2Cu_3O_{7-\delta}$ as the top layer, while maintaining $La_{2-x}Sr_xCuO_4$ as the bottom layer. The

first type of bilayer is grown as described in Section 3.3.3, and leads to limited ΔT_c. We concentrated most of our efforts in the second type of bilayer, as $YBa_2Cu_3O_{7-\delta}$ is known to have a substantially higher T_c than $La_{2-x}Sr_xCuO_4$ (bulk values of 93 K [133]), with which ΔT_c can be maximized. An etched bilayer sample is made by first growing the bilayer by means of PLD, followed by a electron beam lithography process to define the areas which are to be etched.

The bilayers are grown on $LaSrAlO_4$ substrates to facilitate layer-by-layer growth of the initial, $La_{2-x}Sr_xCuO_4$ layer (see Fig. 3.15a(top)). The deposition parameters of $La_{2-x}Sr_xCuO_4$ are the same as those described in Section 3.3.3. The growth of $La_{2-x}Sr_xCuO_4$ is followed by that of $YBa_2Cu_3O_{7-\delta}$ at a slightly higher temperature and oxygen background pressure, 780 C and 2.0×10^{-1} mbar, respectively. Growing $YBa_2Cu_3O_{7-\delta}$ at a slightly lower temperature of 720 C stimulates a-axis growth of $YBa_2Cu_3O_{7-\delta}$, which is unwanted. The laser fluence is 1.3 J/cm^2 with a repetition rate of 1 Hz, while the target-substrate distance is held at 50 mm. As can be seen in Fig. 3.15a(top), the clear oscillations facilitated by a 2D growth mode is dampened considerably with the growth of $YBa_2Cu_3O_{7-\delta}$, suggesting a 3D growth mode. RHEED oscillations are typically unobservable after the completion of the 4^{th} UC, accompanied by a spotty RHEED pattern. The 3D growth is likely to be formed by limited mobility of the ablated material on arrival at the substrate surface [167].

To maintain 2D growth for a maximum amount of time, growth interruption in most bilayers is used after the completion of every UC, as is shown in Fig. 3.15a(bottom). This allows for recrystallization and reversing the coarsening of the surface. With this method, up to the 30^{th} UC can be observed by RHEED. At each laser pulse, the intensity of the specular beam drops, accompanied by the increased disorder on the surface. This is immediately followed by an exponential rise due to recrystallization of the initially disordered material (see Fig. 3.15c). The characteristic time of this process, τ, is the decay time of the adatom density on the terraces, as is determined from the recovery of the RHEED intensity. If we take the diffusion length to be limited by the average terrace size of the used substrate (100 nm for a typical miscut angle of 0.2 degrees), the maximum limit of the diffusion constant $D \approx l_t^2/\tau = 2.9\times10^{-12}$ cm^{2}s, as τ is approximately 35 s. This value is in line with known values for $YBa_2Cu_3O_{7-\delta}$ growth on $SrTiO_3$(001) substrates [168]. The RHEED patterns typ-

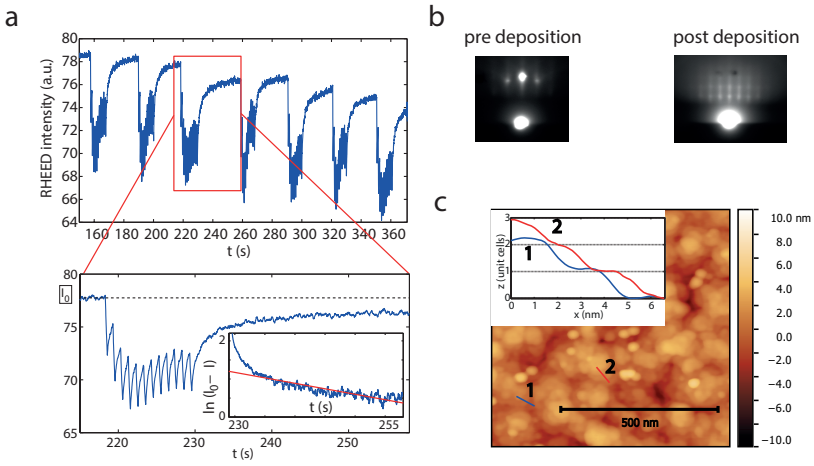

Figure 3.15: **(a)** RHEED vs. time of $YBa_2Cu_3O_{7-\delta}$ growth using growth interruption after the completion of every UC. After every pulse of the laser, the increased disorder induces a drop in the RHEED intensity, which recovers according to an exponential behavior, representing surface crystallization. The time delay connected to this process is 35 s, which is typical of cuprate films grown at this temperature. **(b)** The initial RHEED pattern of the substrate surface changes and becomes spotty after the growth of 30 UCs of $YBa_2Cu_3O_{7-\delta}$. **(c)** A typical AFM image of a $YBa_2Cu_3O_{7-\delta}$ film. The film is coarsened, with individual islands locally showing step heights corresponding to the $YBa_2Cu_3O_{7-\delta}$ c axis lattice parameter, 11.7 Å.

ically show 3D spots on 2D streaks (see Fig. 3.15a). Although the $YBa_2Cu_3O_{7-\delta}$ surface is coarsened (the typical roughness is around 1.4 nm, whereas the substrate roughness is 0.3 nm), it is possible to see UC step heights on the surface of the 3D islands (see Fig. 3.15b).

The main parameter with which the T_c of the $YBa_2Cu_3O_{7-\delta}$ layer is tweaked is the oxygen annealing time at 600 and 450 C, which can vary from 15 to 30 minutes at both annealing temperatures. Table 3.2 gives a summary of the range of thicknesses and T_c's of all bilayers that were used.

The first four $YBa_2Cu_3O_{7-\delta}/La_{2-x}Sr_xCuO_4$ bilayers show a low T_c of the $YBa_2Cu_3O_{7-\delta}$ layer, the bulk value of which is 93 K. These were subjected to a 15 min oxygen annealing at both 600 and 450 C. To test whether this is an inherent growth problem, we grew a single $YBa_2Cu_3O_{7-\delta}$ layer film of 30 UC on an $LaSrAlO_4$ substrate which was annealed for 30 minutes at both temperatures. The T_c of this

Top layer (2)/Bottom layer (1) (Sample number)	t_1 (UC)	t_2 (UC)	$T_{c,1}$ (K)	$T_{c,2}$ (K)	ΔT_c
LSCO(0.15)/LSCO(0.07) (1)	40	7	5	18	13
YBCO/LSCO(0.15) (2)	20	20	28	38	10
YBCO/LSCO(0.15) (3)	20	30	28	35	7
YBCO/LSCO(0.15) (5)	25	31	21	31	10
YBCO/LSCO(0.15) (6)	25	31	17	59	42
YBCO/LSCO(0.07) (8)	30	30	10	78	68

Table 3.2: List of bilayer parameters: sample number and bilayer composition, thickness, T_c of the top and bottom layers, and the corresponding ΔT_c. The doping levels of $La_{2-x}Sr_xCuO_4$ (LSCO) are parenthesized. Here, YBCO stands for $YBa_2Cu_3O_{7-\delta}$.

+

film was 86 K, which is close to the bulk value. Hence, the low T_c is interpreted as the consequence of non-optimal δ in the $YBa_2Cu_3O_{7-\delta}$ film, presumably caused by an insufficient time for oxygen to diffuse into the film. Hence, the final $YBa_2Cu_3O_{7-\delta}/La_{2-x}Sr_xCuO_4$ bilayer is annealed for 30 minutes at both temperatures, and shows an improved T_c , albeit still lower than optimal, but sufficiently high T_c for giant proximity effect studies. As a note, a suppression in T_c of the $YBa_2Cu_3O_{7-\delta}$ layer can also be caused by interfacial strain effects, as 100 nm thick $YBa_2Cu_3O_{7-\delta}/La_{2-x}Sr_xCuO_4$ bilayers show a T_c of 90 K in previous reports [20].

Finally, after fabrication of a resist mask by e-beam lithography, Ar ion bombardment at an acceleration voltage of 350 - 500 V is used to etch away a trench in the top layer at a rate of 6 - 7 nm/min. For this, the PMMA layer used for writing the areas that are to be Ar etched needs to be relatively thick (240 nm). PMMA which has been exposed to Ar ion bombardment tends to change in its properties and is much harder to remove with standard lift-off in acetone and ethanol. Instead, an ethanol wetted lens tissue is used to remove the contaminants.